AERODYNAMIC CHARACTERISTICS OF THE SAGITTA DIAMOND WING DEMONSTRATOR CONFIGURATION

A. Hövelmann, C. Breitsamter
Institute of Aerodynamics and Fluid Mechanics, Technische Universität München
Boltzmannstr. 15, 85748 Garching bei München, Germany

Abstract

The aerodynamic characteristics of a diamond wing shape unmanned aerial vehicle (UAV), the so called SAGITTA demonstrator configuration, are investigated. Reynolds Averaged Navier-Stokes computations as well as wind tunnel force measurements are applied to generate an aerodynamic data set for two different configurations. On the one hand, the diamond wing UAV is considered as tail-less configuration, while on the other hand, a double vertical tail is attached to the SAGITTA demonstrator configuration.

The results of the computed and measured aerodynamic force and moment coefficients and their corresponding derivatives are compared to each other for both the longitudinal and the lateral motion. A good agreement between the numerical and experimental data is observed for both regarded configurations. For the tail-less diamond wing UAV, no lateral yaw stability is present without control surface deflection. Therefore, lateral stability is provided by vertical tails constituting the first flight configuration within the SAGITTA demonstrator program.

NOMENCLATURE

b	[m]	Wing Span
C_D	[-]	Drag Coefficient
C_L	[-]	Lift Coefficient
C_Y	[-]	Side Force Coefficient
C_l	[-]	Rolling Moment Coefficient
C_m	[-]	Pitching Moment Coefficient
C_n	[-]	Yawing Moment Coefficient
c_r	[m]	Root Chord Length
c_t	[m]	Tip Chord Length
h	[m]	Flight Altitude
l_{VT}	[m]	Vertical Tail Height
l_μ	[m]	Mean Aerodynamic Chord / Longitudinal Ref. Length
Ma	[-]	Mach Number
p_∞	$[N/m^2]$	Ambient Pressure
Re	[-]	Reynolds Number
S_{Ref}	$[m^2]$	Reference Area
s	[m]	Wing Half Span / Lateral Ref. Length
T_∞	[°C]	Ambient Temperature
U_∞	[m/s]	Freestream Velocity
α	[°]	Angle of Attack
β	[°]	Sideslip Angle
ϑ	[°]	Roll Angle
ρ_∞	$[kg/m^3]$	Ambient Density
Λ	[-]	Aspect Ratio
λ	[-]	Taper Ratio
φ_{LE}	[°]	Sweep Angle at Leading Edge
φ_{TE}	[°]	Sweep Angle at Trailing Edge
ψ	[°]	Yaw Angle

1 INTRODUCTION

In the early stage of aircraft design, the determination of the aerodynamic characteristics often play a major role. Within the SAGITTA program led by EADS CASSIDIAN, these characteristics are investigated at the Institute of Aerodynamics and Fluid Mechanics (AER) at Technische Universität München (TUM). Launched in 2011, the SAGITTA project focuses on the development of an unmanned aerial vehicle (UAV) with diamond wing shape, resulting in a low-observable wing planform. In the research program, EADS

CASSIDIAN and several partners from German universities and research institutes work on different research topics, to be tested on a scaled model of the diamond wing UAV, the SAGITTA demonstrator configuration [1].

The aerodynamic characteristics of this demonstrator UAV are determined at TUM-AER by comprehensive numerical and experimental investigations, which are presented and compared in this paper. Based on the generated data set, an aerodynamic data module (ADM) is built for the further design process of the SAGITTA demonstrator [2]. It consists of force and moment coefficients for a wide range of angles of attack and sideslip as well as for different configurations. Thus, the ADM contains all relevant information about the aerodynamic characteristics of the SAGITTA demonstrator configuration inside its flight envelope for subsequent use by all partners for their further research within the SAGITTA demonstrator program.

Overall, diamond wing planforms have already been investigated for a long time [3]. However, compared to delta wing configurations without trailing-edge sweep angle, a lot less data and analyses are available in research. In recent years, diamond wing configurations have become more important again, since the research on future UAV also focuses on this type of wing planform [4]. The presence of a non-zero trailing-edge sweep angle at diamond wing shapes is mainly caused by low-observability requirements for UAV configurations. As a result of the high leading-edge sweep angle, though, the aerodynamic characteristics of diamond wing planforms are quite similar to delta wing configurations. Aerodynamic potential and high maneuverability known from delta wing configurations are of particular interest and therefore generally maintained for diamond wing shapes.

2 THE SAGITTA DEMONSTRATOR CONFIGURATION

Based on preliminary studies performed by EADS CASSIDIAN in the forefront of the research program, the wing planform of the SAGITTA UAV has been defined as a diamond wing shape featuring a 55° leading-edge sweep and a 25° trailing-edge sweep angle. The scaled SAGITTA demonstrator configuration, which is addressed in this publication, exhibits a wing span of $b = 3.088\ m$ and a root chord of $c_r = 3\ m$. Due to practical reasons, the wing tip chord has been set to $c_t = 0.075\ m$. Table 1 summarizes all relevant geometry information about the SAGITTA demonstrator UAV, while Figure 1 shows the wing planform of the SAGITTA demonstrator configuration.

b	[m]	3.088	φ_{LE}	[°]	55
c_r	[m]	3.000	φ_{TE}	[°]	-25
c_t	[m]	0.075	λ	[-]	0.025
S_{Ref}	[m^2]	4.748	Λ	[-]	2.010
l_μ	[m]	2.001			

Table 1: Wing planform parameters of the SAGITTA demonstrator configuration.

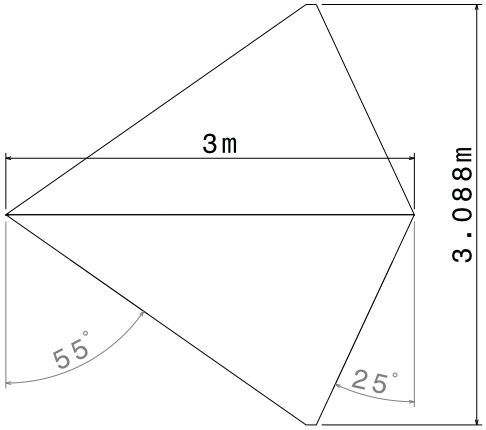

Figure 1: Wing planform of the SAGITTA demonstrator configuration.

As a result of relevant constraints within the SAGITTA research program, the airfoil of the demonstrator configuration is to be of symmetric type with 12% relative thickness. Thus, a symmetric NACA64A012 airfoil has been chosen for the demonstrator configuration. However, the airfoil has been modified in the inboard wing section, i.e. within the inner 20% of the wing half span. On the one hand, the airfoil has been slightly thickened in the rear part due to installation space requirements. On the other hand, the blunt leading edge of the NACA airfoil has been replaced by a sharp leading edge. This geometry modification already leads at moderate angles of attack to a predefined flow separation and consequently to the formation of distinctive vortex structures in the inboard wing section [5]. For blunt leading-edges, the vortex formation becomes generally more complicated and depends on several parameters [6, 7].

In contrast to slender delta and diamond wing shapes with thin airfoils [8], however, the flow effects due to vortex systems are not as relevant for this non-slender diamond wing shape with 12% relative thickness [9]. The influence of the inboard vortex systems does not dominate the flow field around the diamond wing shape until the angle of attack reaches α-values near the boarder of the flight envelope of the SAGITTA demonstrator configuration. Therefore, this paper does not focus on vortex effects, but on the aerodynamic characteristics of the demonstrator UAV inside its intended flight envelope.

Generally speaking, the SAGITTA configuration only consists of its flying wing body, but due to low-observability reasons it exhibits no vertical tail. Possible instabilities in both the longitudinal and the lateral motion shall only be handled by the control surfaces [10] and a thrust-vectoring system, which is also researched within the SAGITTA program [11]. For safety reasons, however, a double vertical tail has been added in the preliminary design phase to the demonstrator configuration in order to guarantee lateral stability for the first flight tests. Based on preliminary design methods, the planform of the vertical tails has been estimated and sized. As airfoil type, a symmetric NACA 64A008 has been defined. Hence, the aerodynamic characteristics for the demonstrator configuration with attached vertical tails is also requested for the SAGITTA ADM and is regarded as well in this paper. Figure 2 displays an isometric view of the SAGITTA demonstrator configuration with attached vertical tails, while the resulting planform parameters of the vertical tail are shown in Table 2.

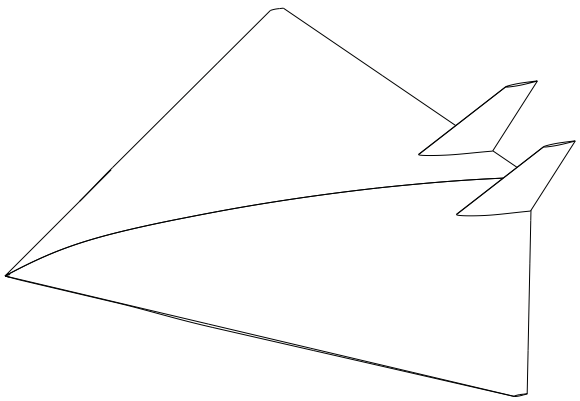

Figure 2: Isometric view of the SAGITTA demonstrator configuration with vertical tails.

l_{VT}	[m]	0.440	$\varphi_{LE,VT}$	[°]	50
$c_{r,VT}$	[m]	0.520	$\varphi_{TE,VT}$	[°]	22.75
$c_{t,VT}$	[m]	0.180	λ_{VT}	[-]	0.345
$S_{Ref,VT}$	[m^2]	0.154	Λ_{VT}	[-]	1.257

Table 2: Vertical tail planform parameters of the SAGITTA demonstrator.

3 NUMERICAL METHODS

3.1 Mesh Generation

In order to investigate the aerodynamic characteristics of the SAGITTA demonstrator configuration by computational fluid mechanics (CFD), an appropriate mesh must be generated as input for the flow solver of choice. In the present analysis, the hybrid mesh generator CENTAUR by CentaurSoft has been used for the mesh generation process. Based on an unstructured surface mesh consisting of triangles and quadrilaterals, prismatic and hexahedral elements are used in hybrid meshes close to the configuration so the boundary layer can be resolved with very fine cells. Elsewhere in the computational domain, which extends in the present analysis ten wing spans in each direction around the configuration, tetrahedral elements are used.

In order to reach a y^+-value of $y^+ \approx 1$ on the surfaces of the configuration, which is desired for Reynolds Averaged Navier-Stokes (RANS) turbulence models, the resolution of the prismatic mesh must be chosen adequately. Based on 30 prism layers and a stretching factor of 1.308, the height of the initial layer thickness in normal direction has been estimated for the SAGITTA demonstrator configuration to be 0.004 mm. With these input values, hybrid meshes have been generated for both the tail-less demonstrator configuration ("Clean") and the configuration with attached vertical tails ("VT Clean"). These meshes, whose approximate sizes are summarized in Table 3, have been used for the numerical computations presented in this paper.

	Surface Grid	Prismatic Grid	Hybrid Grid
Clean	$\approx 360 \cdot 10^3$	$\approx 11.3 \cdot 10^6$	$\approx 14.5 \cdot 10^6$
VT Clean	$\approx 517 \cdot 10^3$	$\approx 16.2 \cdot 10^6$	$\approx 20.7 \cdot 10^6$

Table 3: Approximate mesh size (number of elements) of the considered configurations.

Furthermore, basic sketches of the generated surface meshes are shown in Figure 3 and Figure 4. As example for the tail-less configuration, the whole surface mesh is displayed, whereas for configuration VT Clean, only a detailed view of the attached vertical tails is presented.

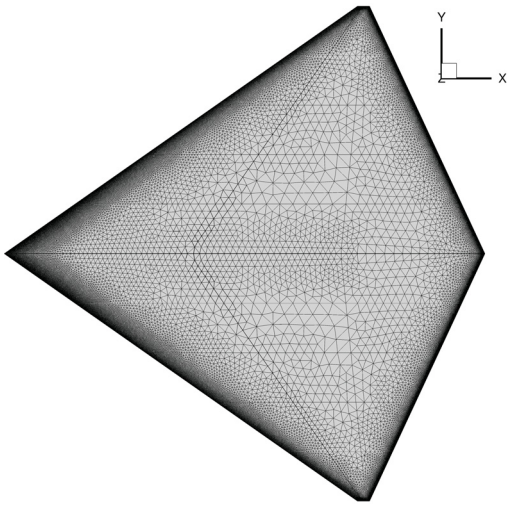

Figure 3: Surface mesh of the SAGITTA demonstrator configuration without vertical tails.

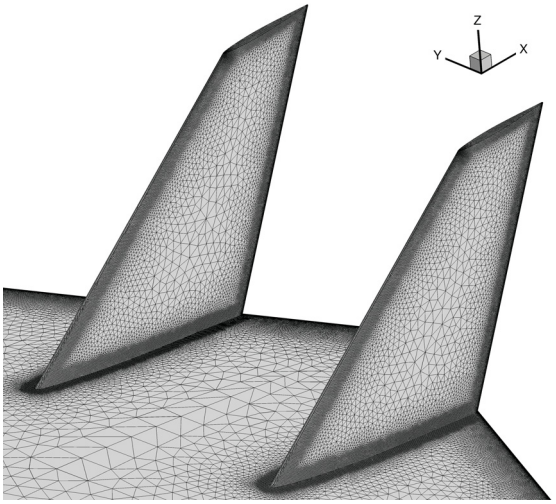

Figure 4: Surface mesh of the attached vertical tails (configuration VT Clean).

3.2 Flow Solver and Numerical Setup

The CFD computations conducted during the course of the numerical investigations of the SAGITTA demonstrator configuration have been performed with the DLR TAU-Code. It solves the three-dimensional compressible Reynolds Averaged Navier-Stokes (RANS) equations, is based on a finite volume scheme and uses a dual-grid approach [12]. Furthermore, it is developed to compute the RANS equations on hybrid unstructured meshes in parallel mode.

In the present analysis, the one-equation turbulence model by Spalart-Allmaras has been applied to the RANS equations in its original version (SAO) [13]. For the finite volume discretization, a second-order central scheme with scalar dissipation has been used, while for the discretization in time, an implicit Backward-Euler scheme with LUSGS algorithm has been applied. The convergence of the computations has been accelerated by a multigrid technique as a 3v-cycle has been used. The computations have been performed in parallel mode with up to 160 cores.

The CFD analyses presented in this paper have been conducted for the cruise condition of the SAGITTA demonstrator configuration carrying out steady-state computations. Designed for subsonic speeds of up to about $Ma_{Max} \approx 0.35$ and a ceiling height of $h_{Max} = 2500\ m$, the cruise condition of the demonstrator UAV has been defined to $Ma_{Cruise} = 0.3$ and $h_{Cruise} = 1000\ m$. Based on the mean aerodynamic chord (MAC) of the diamond wing configuration (noted in Table 1), the cruise Reynolds number results in $Re_{Cruise} = 12.7e6$. The reference point for the moment calculation has been set to the geometrical neutral point of the wing at $\vec{X} = [1.253, 0, 0]\ m$ behind the nose, which almost coincides with the desired center of gravity of the SAGITTA demonstrator. Thus, the computed moment coefficients result in meaningful values for stability analyses.

The numerical investigations have been arranged further for pure α- and β-polars at zero sideslip angle and zero angle of attack, respectively. Thus, the range of computed angles of attack at $\beta = 0°$ reads $\alpha = [0°; 18°]$, while the lateral analyses are based on CFD results at $\alpha = 0°$ and $\beta = [0°; 14°]$. The maximum α- and β-values have thereby been chosen with some safety margin due to relevant constraints within the flight envelope of the SAGITTA demonstrator configuration (cross wind requirements and desired landing speed). As a result of symmetry reasons of the SAGITTA diamond wing, the computed force and moment coefficients of the β-polar have additionally been mirrored to negative sideslip angles for both demonstrator configurations considered in this paper (Clean and VT Clean). In contrast, the results of the α-polar have only been mirrored to negative angles of attack for the tail-less configuration (Clean), since the attached vertical tails break up the symmetry of the VT Clean configuration around the x-y plane.

4 WIND TUNNEL EXPERIMENTS

4.1 Wind Tunnel Facility and Model

The experimental analyses of the SAGITTA demonstrator configuration have been performed in the wind tunnel facility A of TUM-AER. The Göttingen-type low-speed wind tunnel has an open test section with the dimensions (height x width x length) of $1.8\ m$ x $2.4\ m$ x $4.8\ m$. The maximum velocity of the open wind tunnel is $U_\infty = 65\ m/s$, but due to blockage effects of the model, the maximum usable velocity can be slightly lower.

For the wind tunnel tests, a 1:3-scaled model of the SAGITTA demonstrator configuration has been built. The resulting root chord length is $c_{r,WT} = 1\ m$, the wing span reads $b_{WT} = 1.029\ m$ and the wing reference area results in $S_{Ref,WT} = 0.528\ m^2$. The model manufactured of fiber glass is equipped not only with removable vertical tails, but also with attachable landing gears; control surfaces for pitch, roll and yaw control are also incorporated in the model, continuously adjustable via model servos so that various flight maneuvers can be measured. Rear mounted on the model's root section, the wind tunnel model has been held in the test section by a sting support, Figure 5.

For measuring various angles of attack α and sideslip angles β, a roll-yaw-mechanism of the sting support has been used, which can be operated fully automatically. The roll angle ϑ and the yaw angle ψ, which can be adjusted computer-controlled, are mapped onto α and β by

$$(1) \quad \alpha = \arctan 2\left(\sin\psi \sin\vartheta, \cos\psi\right) \qquad \in [-\pi;\pi]$$

$$(2) \quad \beta = \arcsin\left(\sin\psi\cos\vartheta\right) \qquad \in \left[-\frac{\pi}{2};\frac{\pi}{2}\right].$$

4.2 Force Measurements

The forces and moments acting on the wind tunnel model have been measured by an external six-component strain gauge balance located below the wind tunnel test section. In order to correctly refer the moment components to the geometrical neutral point of the wind tunnel model (defined in concordance with the demonstrator configuration, but scaled), the measured force and moment components have been transformed automatically during data processing from the strain gauge balance reference point to the wind tunnel model reference point. Thus, the experimental measured moments can easily be compared to the established numerical data.

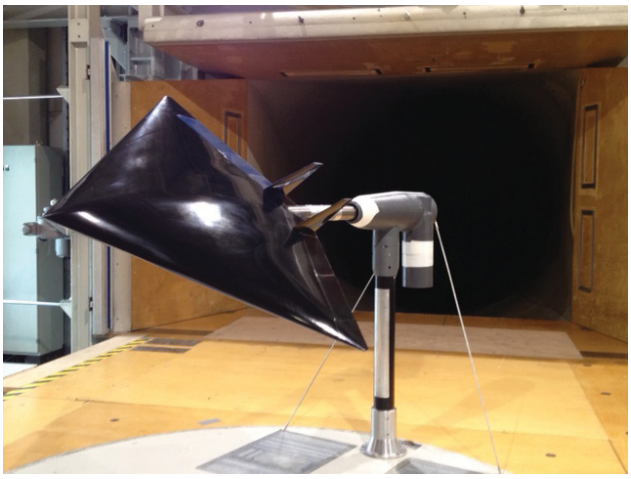

Figure 5: Wind tunnel model with sting support.

Due to a cover of the sting support, which has not been connected at all to the sting itself, the force and moment components acting on the sting cover have not been measured in the experiments by the strain gauge balance. Thus, only static calibrations with the influence exerted by gravity effects of the wind tunnel model are needed depending on the desired α-β-combinations. Additional dynamic calibrations have therefore been unnecessary. This method has turned out to be very convenient for generating an aerodynamic dataset with numerous data points to measure.

However, owing to practical reasons observed within the wind tunnel experiments, the sting cover has not been continued exactly up to the trailing edge of the wind tunnel model as intended at first, Figure 5. Thus, about 30cm of the sting have not been protected by the sting cover and have therewith contributed to the force and moment measurements. This should be kept in mind for the further analysis of the experimental data (see also Section 5.3), as some effects of this experimental set-up must be expected in the lateral degree of freedom.

4.3 Test Conditions, Measurement Ranges and Considered Configurations

The force measurements of the SAGITTA demonstrator wind tunnel model have been conducted at a velocity of $U_\infty = 40\ m/s$ at ambient pressure p_∞ and ambient temperature T_∞, which have slightly varied between the experiments. Based on the model's MAC of $l_{\mu,WT} = 0.667\ m$, the Reynolds number of the wind tunnel tests is $Re_{WT} \approx 1.7e6$ and the corresponding Mach number is $Ma_{WT} \approx 0.12$.

According to predefined requirements within the SAGITTA demonstrator program (see Section 3.2), the measurement range of α-β-combinations has been set to angles of attack of $\alpha = [-18°; 18°]$ and sideslip angles of $\beta = [-14°; 14°]$. In contrast to the CFD computations, the experimental force measurements have been performed for positive and negative angles of attack and sideslip angles, respectively.

Overall, force measurements have been arranged for the tail-less configuration (Clean), the configuration with attached vertical tails (VT Clean) and the landing configuration with extended landing gears. In addition, each of the control surfaces for roll, pitch and yaw control has been tested thoroughly for different flap deflections. A total number of more than 7500 data points has been covered within the wind tunnel experiments, which are to be used for the aerodynamic data module (ADM). As initially discussed above, only the results of the two different clean configurations (Clean and VT Clean) are presented in this paper, whereas the analysis of the control surfaces and the landing configuration is not be regarded in the present publication.

5 Results and Discussion

This section discusses and compares the results of the numerical analyses and the experimental investigations of the SAGITTA demonstrator configuration. At first, the definitions of the aerodynamic force and moment coefficients are introduced and briefly explained. Next, the longitudinal motion is regarded. Since the effect of the attached vertical tails is not deemed to be considerable in this degree of freedom, only the tail-less clean configuration is considered. In Section 5.3, the results of both configurations addressed in this paper (Clean and VT Clean) are discussed, since the vertical tails contribute most notably to the lateral motion of the SAGITTA demonstrator UAV. Hence, the effect of attached vertical tails is evaluated by means of the comparison of side force coefficients as well as rolling and yawing moment coefficients.

Overall, the Reynolds similarity between numerics and experiment is not valid in the present analysis as about one order of magnitude lies between both Reynolds numbers ($Re_{WT}/Re_{CFD} \approx 0.13$). This fact is caused by the scaled wind tunnel model and the maximum available test velocity within the wind tunnel experiments. For the following presentation of the results, this aspect must be considered.

5.1 Aerodynamic Force And Moment Coefficients

In order to compare the aerodynamic force and moment coefficients to each other, the computed and measured body-fixed forces and moments have been transformed to a wind-fixed aerodynamic reference frame. Within this frame, the x-axis points backwards in the direction of the freestream velocity, while the y-axis points rightwards and the z-axis upwards. The aerodynamic moments are defined in a right-hand system, which corresponds to the positive axis directions as introduced above. Furthermore, the forces and moments have to be made dimensionless with appropriate reference quantities. Based on the aerodynamic forces lift (L), drag (D) and side force (Y) as well as the aerodynamic moments rolling moment (l), pitching moment (m) and yawing moment (n), the corresponding coefficients are defined with the dynamic pressure q_∞ as follows:

$$q_\infty = \frac{1}{2} \cdot \rho_\infty \cdot U_\infty^2 \tag{3}$$

$$C_D = \frac{D}{q_\infty \cdot S_{Ref}} \tag{4}$$

$$C_Y = \frac{Y}{q_\infty \cdot S_{Ref}} \tag{5}$$

$$C_L = \frac{L}{q_\infty \cdot S_{Ref}} \tag{6}$$

$$C_l = \frac{l}{q_\infty \cdot S_{Ref} \cdot s} \tag{7}$$

$$C_m = \frac{m}{q_\infty \cdot S_{Ref} \cdot l_\mu} \tag{8}$$

$$C_n = \frac{n}{q_\infty \cdot S_{Ref} \cdot s} \tag{9}$$

5.2 Longitudinal Motion

5.2.1 Drag Coefficient

The drag coefficient C_D of the SAGITTA demonstrator clean configuration is analyzed first. In Figure 6, the obtained C_D-values versus the angle of attack α for zero sideslip angle $\beta = 0°$ are shown. Both the numerical (CFD) and the experimental (WTT) data are illustrated. It is apparent that the overall agreement between both data sets is quite good. However, the drag coefficient curve corresponding to the experimental values is slightly shifted to smaller C_D-values for small and moderate angles of attack in comparison to the computed numerical data set. At $\alpha = 0°$, the values of the zero drag coefficient $C_{D,0}$ result in $C_{D,0,WT} = 0.0047$ and $C_{D,0,CFD} = 0.0071$, respectively. Hence, the drag coef-

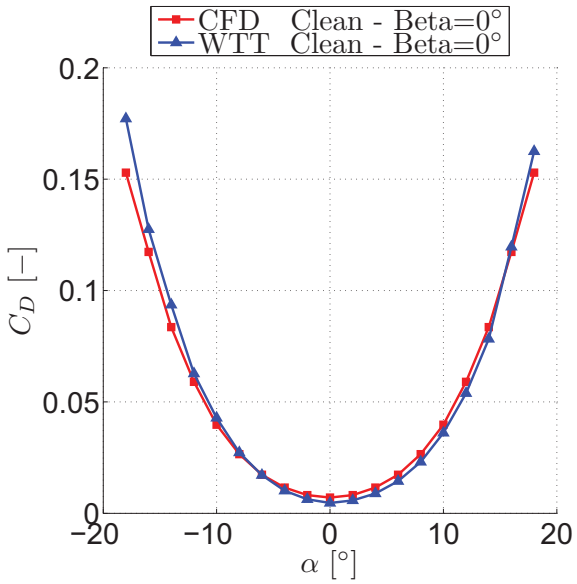

Figure 6: C_D versus α - Clean Configuration.

ficient of the flying wing body is obviously underestimated in the wind tunnel experiments. This can be explained by the difference in the Reynolds numbers between the CFD computations and the conducted wind tunnel measurements as introduced above. While the CFD analyses have been computed fully turbulent, the boundary layer of the wind tunnel model exhibits apparently some laminar regions with smaller skin friction, which leads to the reduced drag coefficient values.

At high angles of attack ($\alpha = 16°$ and $\alpha = 18°$), the numerical drag coefficient values are found to increase less strongly than the experimental values, which show higher drag coefficients in this region. At these α-values, separation effects at the diamond wing tips and vortex structures in the inboard wing section become more and more dominant, which also influences the convergence behaviour of the CFD computations. In addition, unsteady effects play a larger role, which have not been considered in the numerics. Within the experiments, every data point has in contrast been measured and averaged over 15 seconds. Hence, one can expect larger differences in the force and moment coefficients with increasing angles of attack.

As mentioned before in Section 3.2, the numerical data set has been mirrored to negative angles of attack, whereas the experimental data has been measured for negative α-values as well. Comparing both the positive and the negative branches of the drag coefficient curves, it can be noticed that the measured drag coefficient curve is not fully symmetric around $\alpha = 0°$, contrary to the CFD data. At negative angles of attack, slightly higher drag coefficients are noticed. This observation indicates a small asymmetry of the SAGITTA wind tunnel model with respect to the x-y plane or rather small deficiencies in the correct positioning of the wind tunnel model within the test section.

5.2.2 Lift Coefficient

Figure 7 plots the lift coefficient C_L of the SAGITTA demonstrator UAV versus the angle of attack α. In order to point out some flow effects more clearly, Figure 7 also includes illustrations of computed field streamlines around the diamond wing configuration for different α-values.

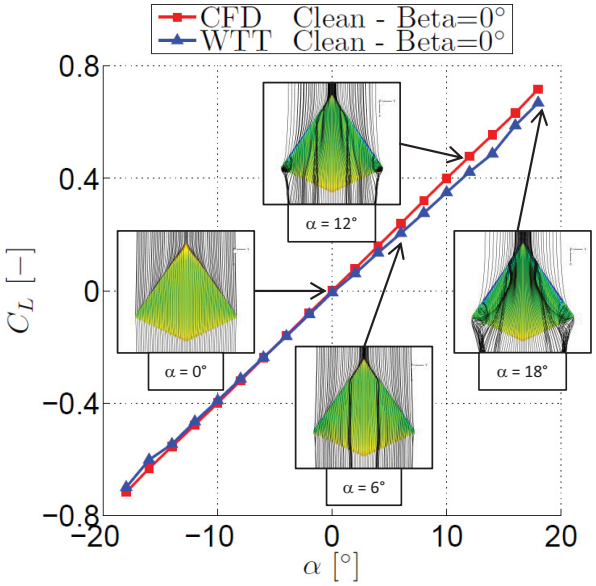

Figure 7: C_L versus α - Clean Configuration.

The overall characteristics of the lift coefficient curves are described in a very similar way by both the CFD and the WTT data. However, the lift coefficient curve observed experimentally for the positive α-branch slightly diverges from the computed C_L-α curve with increasing angles of attack, whereas the agreement between the data sets for the negative α-branch is better. This observation can be more clarified as the lift slope $C_{L,\alpha}$ is displayed versus the angle of attack, Figure 8. It can be clearly noticed that for moderate angles of attack of up to about $\alpha \leq \pm 8°$, the agreement between the CFD data and the WTT data is much better for negative than for positive angles of attack. The global level

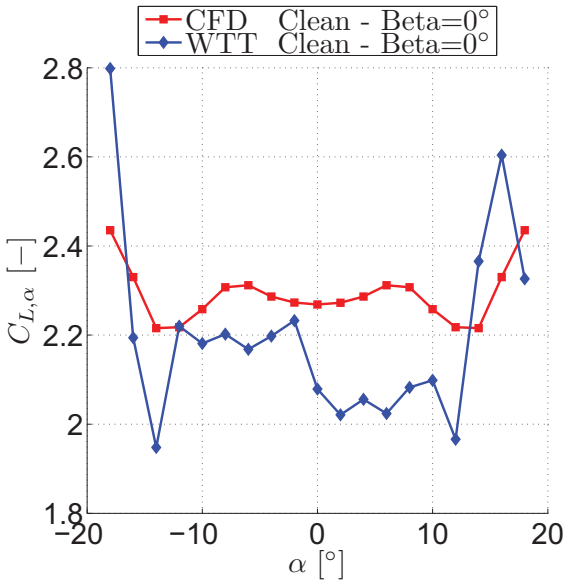

Figure 8: $C_{L,\alpha}$ versus α - Clean Configuration.

of the lift slope observed within the computations is about $C_{L,\alpha} \approx 2.3$, while the experimental lift slope results in about $C_{L,\alpha} \approx 2.2$ on the negative and about $C_{L,\alpha} \approx 2.05$ on the positive α-branch.

Considering the field streamlines in Figure 7, it can be noticed that the vortices in the inboard wing section are already present at $\alpha = 6°$. At this angle of attack, however, no dominant influence of the vortices on the lift characteristics is observed, since the regions of low pressure at the vortex core axes are not yet strongly developed. Thus, only a small increase of the computed lift slope $C_{L,\alpha}$ can be seen in Figure 8 for small angles of attack. This effect, not observed for the experimental data, is mainly caused by the different Reynolds numbers. Following, it can be assumed that the formation of the vortex structures is Reynolds-dependent for the present diamond wing UAV.

The decrease in the lift slope at angles of attack of $\alpha \geq 8°$ and $\alpha \geq 10°$, respectively, which can also be observed from Figure 8, is caused by the evolving separations at the diamond wing tip sections. As shown in Figure 7, the streamlines indicate no separation regions at the wing tips up to $\alpha = 6°$. At an α-value of $\alpha = 12°$, in contrast, separation regions are clearly noticeable at the diamond wing tips. Beginning at $\alpha \geq 8°$, these regions of separated flow increase with increasing angle of attack, which leads to a decreased lift slope $C_{L,\alpha}$. This effect is observed for both the CFD and the WTT data. Moreover, up to an α-value of $\alpha \leq 12°$ and $\alpha \leq 14°$, respectively, the effect of separation regions at the wing tip sections is seen to be more powerful than the lift-increasing effect of the inboard vortex systems.

If the angle of attack is even further increased, the lift slope $C_{L,\alpha}$ starts to increase again and continuously for the CFD data. This observation is also explained by the influence of the vortex structures in the inboard wing section. With increasing angle of attack, the leading-edge vortices become more dominant and their effect on the lift characteristics of the SAGITTA demonstrator UAV is now stronger than the effect caused by the wing tip separations. Highlighted by the streamlines for $\alpha = 12°$ and $\alpha = 18°$ in Figure 7, the vortex structures are clearly noticeable and more distinctive than for $\alpha = 6°$. In addition, low pressure regions are observed in the vicinity of the sharp trailing edge, which are mainly responsible for the vortex generated lift contribution. Because of several aspects concerning vortex aerodynamics as introduced in Section 2 (non-slender diamond wing, 12 % relative airfoil thickness), however, the non-linear lift contribution due to flow-dominating vortices does not turn out to be very strong for the SAGITTA demonstrator configuration. Considering once again the computed lift coefficient curve in Figure 7, a pronounced non-linear behaviour can not be recognized. If the angle of attack would be increased even more, the non-linear lift contribution would presumably increase and could be analyzed more thoroughly.

Comparing the experimental lift coefficient data at negative and positive angles of attack around $\alpha \geq \pm 12°$, a diffusive behaviour is observed. In concordance with the CFD data, the lift slope starts to increase again at $\alpha = 12°$, but no continuous trend for negative and positive angles of attack is noticed. The increase of $C_{L,\alpha}$ is much more distinctive than for the CFD data, but the trend is not continuous in the positive α-branch. Corresponding to the observations in the lift slope, small kinks are noticed for the experimental data at high positive and negative angles of attack in Figure 7. In order to explain the different behaviour in comparison to the CFD data, the Reynolds number dependence of the vortex systems is stated again. For a more detailed explanation, CFD data at a comparable Reynolds number would be therefore of high interest. Moreover, possible interference effects between the vortex systems and the sting behind the model must be expected. Thus, the agreement of the lift slope $C_{L,\alpha}$ at high angles of attack between numerics and the experiment is not as good as for small α-values.

5.2.3 Pitching Moment Coefficient

In order to conclude the longitudinal analysis of the SAGITTA demonstrator clean configuration, the pitching moment coefficient C_m is considered below. Figure 9 presents the results of both the numerics and the experiment. As introduced in Section 3.2 and Section 4.2, the C_m-values are referred to the geometrical neutral point of the configuration, which is located at 41.6% of the root chord.

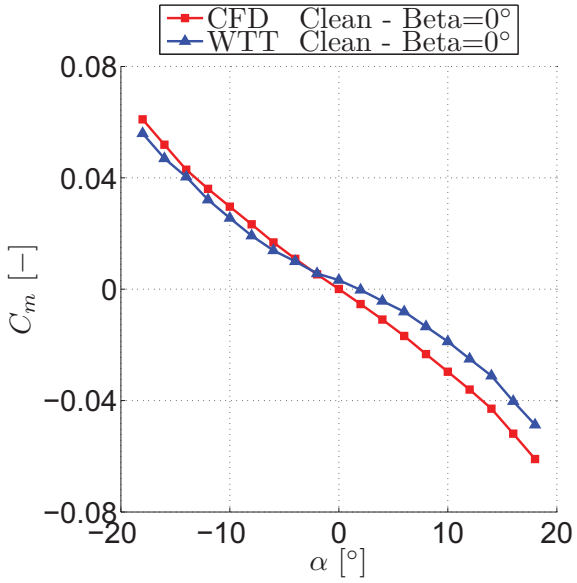

Figure 9: C_m versus α - Clean Configuration.

Both the CFD and the WTT data show smaller C_m-values with increasing angle of attack, which explains the negative slope $C_{m,\alpha}$ of the curves observed. This indicates a stable behaviour of the SAGITTA demonstrator clean configuration in the longitudinal degree of freedom. Furthermore, the agreement between the CFD data and the WTT data is once again more accurate at negative angles of attack. This observation is directly associated with the findings presented in the previous subsection for the lift coefficient as the pitching moment coefficient originates particularly from the lift coefficient.

Since the clean configuration without attached vertical tails is symmetric with respect to the x-y plane, a $C_{m,0}$-value of $C_{m,0} = 0$ at $\alpha = 0°$ is further expected. However, this is only seen with the numerical results, whereas the wind tunnel experiment shows a small positive $C_{m,0}$-value. No exact observation is found for this deficit in the experimental values. In addition, the computed pitching moment coefficients exhibit by and large more linear characteristics than the measured data set. With increasing absolute values of the angle of attack, the slope of the C_m-curves increases, but the increase is much more distinctive for the experimental values than for the CFD data. This effect is highlighted in Figure 10, where the slope of the pitching moment curves, the stability derivative $C_{m,\alpha}$, is plotted versus the angle of attack. It can be noticed that the difference of the $C_{m,\alpha}$-values is quite large at $\alpha = 0°$, but for higher positive and negative α-values, the agreement becomes much better.

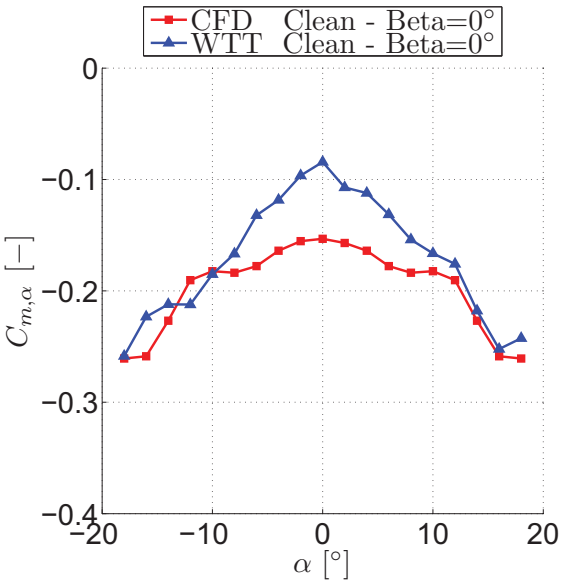

Figure 10: $C_{m,\alpha}$ versus α - Clean Configuration.

5.3 Lateral Motion

5.3.1 Side Force Coefficient

The results concerning the lateral motion of the SAGITTA demonstrator configuration are presented below. First of all, the side force coefficient C_Y is analyzed for both configurations considered in this paper (Clean and VT Clean). The resulting values of numerics and experiment are shown in Figure 11, which plots the coefficients versus the angle of sideslip β at zero angle of attack. Regarding the tail-less configuration (Clean), it can be seen that the flying-wing body produces almost no side force with increasing angle of sideslip, since the projected surface area that is exposed to the cross wind flow is very small. In contrast to classical wing-body configurations with a fuselage, for which the projected surface area drastically increases in cross wind flow,

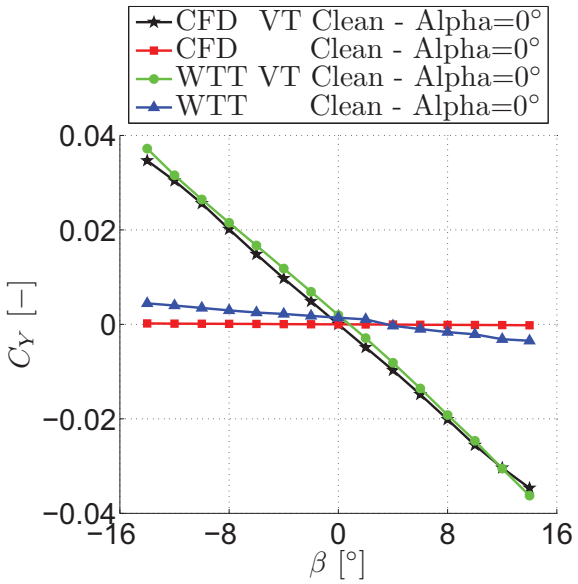

Figure 11: C_Y versus β - Clean & VT Clean Configuration.

the projected surface area of the SAGITTA diamond wing is even reduced at non-zero sideslip angles. Thus, the results of the CFD data indicate C_Y-values close to zero for all sideslip angles considered. In contrast, the experimental side force coefficients of the tail-less configuration show small C_Y-values for non-zero angles of sideslip, which also exhibit a relatively constant gradient over the β-sweep. This effect is explained by the influence of the non-covered sting part in the vicinity of the wing's trailing edge, as mentioned in Section 4.2. For measurements with a present angle of sideslip, the non-covered sting part is slightly exposed to the flow and contributes therewith to the force measurements of the flying wing configuration. For future analyses with the SAGITTA demonstrator wind tunnel model, this effect should be eliminated when the sting cover is extended up to the wind tunnel model.

If one compares the side force coefficients C_Y of the configuration with attached vertical tails (Clean VT) to the aforementioned tail-less configuration, the effect of the vertical tails becomes obvious, Figure 11. The side force coefficients decrease for positive sideslip angles and increase for negative β-values, respectively. Both the CFD and the WTT data show a very good agreement for this configuration. Moreover, the unwanted effect of the non-covered sting part is no longer important, because the side force contribution of the vertical tails dominate the side force coefficient C_Y in its size.

In Figure 12, the derivative of C_Y with respect to the sideslip angle β is shown. In this plot, the side force characteristics can be analyzed more thoroughly. Comparing the CFD data and the WTT data of configuration VT Clean, one can again observe asymmetric effects on the positive and the negative β-branch of the experimental data, which are not present in the CFD data. As mentioned before, small model asymmetries and a probable non-centric positioning within the wind tunnel test section have led to the experimental results presented in this publication. However, manufacturing tolerances must always be considered and can not completely be avoided, so pure symmetric data sets are difficult to obtain. Overall, the global level of the obtained $C_{Y,\beta}$-values varies over the sideslip angle β between $C_{Y,\beta} \approx -0.16$ and $C_{Y,\beta} \approx -0.14$ and fits quite good to the computed $C_{Y,\beta}$-values. For the tail-less configuration named Clean, the above mentioned non-zero gradient for the experimental side force coefficient is furthermore noticed, but the absolute value of the gradient is much smaller than the $C_{Y,\beta}$-values of configuration VT clean.

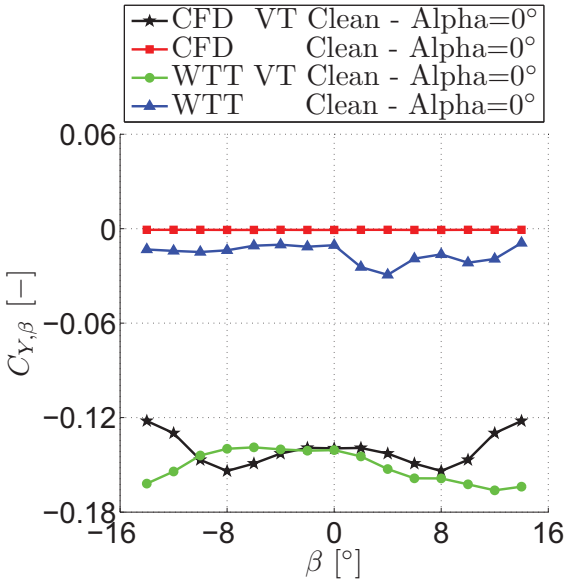

Figure 12: $C_{Y,\beta}$ versus β - Clean & VT Clean Configuration.

5.3.2 Rolling Moment Coefficient

Subsequent to the presentation of the side force coefficient, the rolling moment coefficient C_l is considered next. Figure 13 depicts the corresponding curves. Generally speaking, for the tail-less configuration, the same aspects as for the

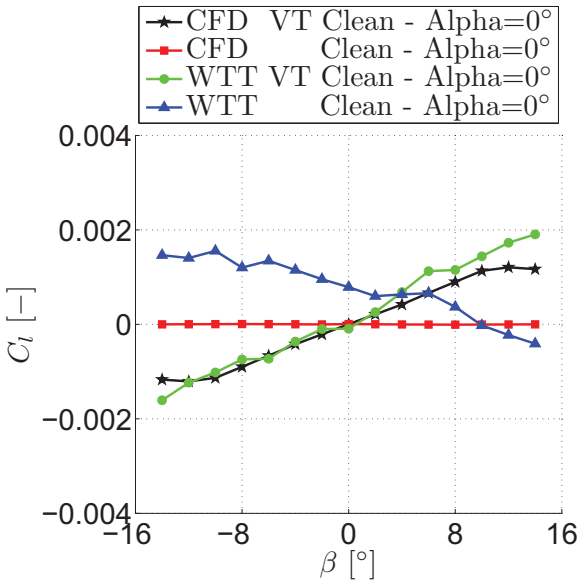

Figure 13: C_l versus β - Clean & VT Clean Configuration.

side force coefficient appear in the resulting analysis. Due to the symmetry of the flying wing body around the x-y plane and the x-z plane, no rolling moment is observed within the CFD data. As a result of small model deficiencies in the wind tunnel model as argued in the previous sections, this curve is not exactly reproduced by the experimental force measurements, Figure 13. In fact, even the rolling moment coefficient at $\beta = 0°$ does not result in a C_l-value of $C_l \approx 0$ and hence, the curve seems to be slightly shifted up.

If the vertical tails are attached to the SAGITTA demonstrator UAV, the symmetry around the x-y plane becomes obsolete. For non-zero sideslip angles, a side force is generated at the vertical tails that acts with a lever arm around the moment reference point located in the symmetry plane of the diamond wing. Hence, the vertical tails generate a non-zero rolling moment if a sideslip angle is present. The comparison of numerics and experiment now agree quite well, Figure 13. However, the experimental values once again show asymmetric tendencies over the β-sweep, resulting in a better agreement for the negative angles of sideslip than for positive β-values. For the configuration with attached vertical tails, the computed zero-rolling moment at $\beta = 0°$ is also affirmed by the wind tunnel experiment, as the rolling moment coefficient results at $\beta = 0°$ in a C_l-value of $C_l = 0$. Moreover, the corresponding derivative $C_{l,\beta}$ yields an averaged value of approximately $C_{l,\beta} \approx 0.06$ over the β-sweep for both the CFD and the WTT data.

If only the experimental results of both regarded configurations are compared to each other, different signs in the slope of the curves are noticed. While the rolling moment coefficient curve of configuration VT Clean is confirmed by the numerics and is expedient due to the effective force directions acting on the vertical tails, the slope of the experimental C_l-curve obtained for the tail-less configuration can not be explained. In addition, the absolute difference in the C_l-values of configuration Clean for $\beta \pm 14°$ is about 50% of the maximum ΔC_l of Configuration VT. For this result, no explanation is found, since the generated side force coefficients of the tail-less diamond wing are considerably smaller compared to configuration VT Clean, as presented in Section 5.3.1. Thus, the effect of attached vertical tails should be much more distinctive, which is however only shown by the numerical results.

5.3.3 Yawing Moment Coefficient

Finally, the results obtained for the yawing moment coefficient C_n are presented below. Figure 14 illustrates the corresponding C_n-curves of the SAGITTA demonstrator UAV for both regarded configurations (Clean and VT Clean) versus the angle of sideslip β.

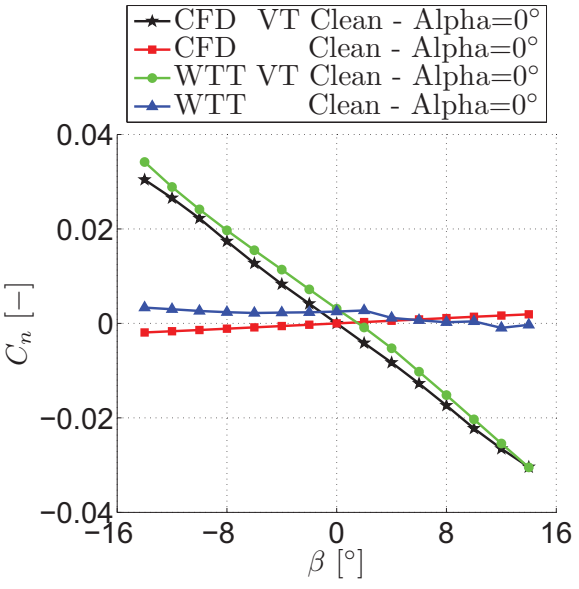

Figure 14: C_n versus β - Clean & VT Clean Configuration.

In contrast to the rolling moment coefficient, the yawing moment coefficient C_n also becomes non-zero at present sideslip angles for the tail-less demonstrator configuration,

which can clearly be observed by the numerical results of configuration Clean. The associated slope of the curve that is equivalent to the stability derivative $C_{n,\beta}$ is found to be slightly positive for the tail-less diamond wing. This effect is caused by the chosen geometry planform of the SAGITTA demonstrator UAV. Figure 15, in which the stability derivative $C_{n,\beta}$ is plotted versus the sideslip angle β, is additionally introduced for further discussion.

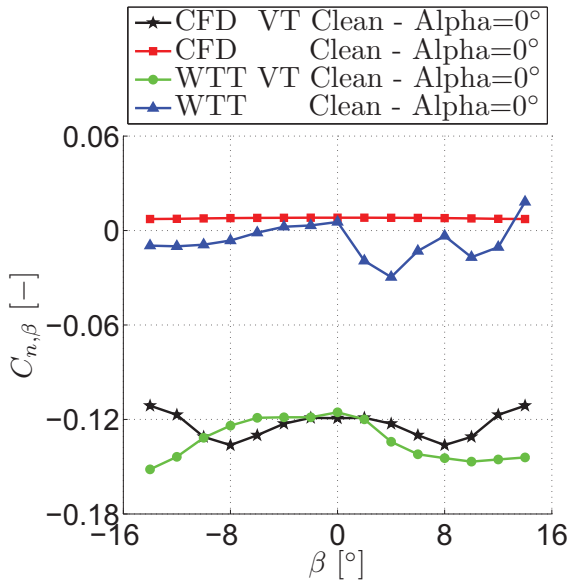

Figure 15: $C_{n,\beta}$ versus β - Clean & VT Clean Configuration.

Within this figure, one can note the small positive $C_{n,\beta}$-values of the CFD data for configuration Clean. Based on the defined coordinate system as explained in Section 5.1, a positive $C_{n,\beta}$-value indicates that the configuration is unstable in the lateral degree of freedom. Following, no weathercock stability is achieved for pure lateral motion at $\alpha = 0°$ for the tail-less SAGITTA demonstrator configuration.

At this stage, the necessity of the attached vertical tails becomes apparent, if the observed instability of configuration Clean is not resolved by thrust-vectoring or the usage of lateral control surfaces. Analyzing the results of configuration VT Clean in Figure 14 and Figure 15, the yawing moment coefficients now result in significant higher values with increasing sideslip angles and exhibit a negative slope. Hence, the stability derivative $C_{n,\beta}$ is also negative. The attached vertical tails thus help the diamond wing configuration to become stable in the lateral degree of freedom for zero angle of attack. For the first flight tests within the SAGITTA demonstrator program, this weathercock stability is much appreciated. Therefore, the achieved $C_{n,\beta}$-values of approximately $C_{n,\beta} \approx -0.12$ to $C_{n,\beta} \approx -0.15$ provide enough safety margin to operate the demonstrator UAV safely in stable flight conditions.

At the very end, the characteristics of the yawing moment coefficients are compared between the computed CFD data and the measured WTT data. In concordance with the observations obtained for the other force and moment coefficients, the agreement between numerics and experiment is better for configuration VT Clean than for configuration Clean. The aforementioned asymmetric effects within the measured data are seen as well for the yawing moment coefficients of both regarded configurations, but the overall agreement between CFD data and WTT data is quite good. Furthermore, it is noticed that for configuration Clean the negative β-branch is notably smoother, which is also observed from the $C_{n,\beta}$-values in Figure 15.

6 Conclusion and Outlook

Both numerical and experimental studies have been investigated on the SAGITTA diamond wing demonstrator configuration to determine its aerodynamic characteristics. Two different configurations have been discussed in this paper, the clean configuration consisting of just the flying wing body (Clean) and the clean configuration with attached vertical tails (VT Clean). For these configurations, numerically computed force and moment coefficients have been compared to experimentally measured values, which have been derived from force measurements on a 1:3-scaled wind tunnel model of the SAGITTA demonstrator UAV.

Overall, the results of the force and moment coefficients discussed show a quite good agreement between the CFD and the wind tunnel data. The most important trends of the aerodynamic characteristics are reasonably predicted and do not differ between the two different methods applied. The experimental data sets, however, are found to exhibit some asymmetric effects that should not be present as a result of geometrical symmetries of the SAGITTA demonstrator. These asymmetries are caused especially at higher angles of attack by unsteady effects due to wing tip separation and vortex systems in the inner wing section, whereas in general also interference effects with the sting support and small model deficiencies are made responsible for obtained discrepancies, particularly in the lateral degree of freedom.

The necessity of vertical tails attached to the flying wing body is pointed out by a stability analysis of both configurations considered for the yawing moment coefficient C_n. Negative $C_{n,\beta}$-values, which indicate weathercock stability in the defined coordinate system, are observed for present sideslip angles at zero angle of attack only with attached vertical tails. If no stabilizing vertical tails are attached, the diamond wing UAV must be laterally stabilized by control surfaces or a thrust-vectoring system.

Beyond the clean configurations of the SAGITTA demonstrator UAV discussed in this publication, a lot more different configurations have been tested in the wind tunnel experiments, but are not further addressed in this paper. Together with the aerodynamic coefficients obtained for deflected roll, pitch and yaw control devices as well as for the landing configuration with extended landing gears, the aerodynamic characteristics of the SAGITTA demonstrator clean configurations form the basis for the generation of the aerodynamic data module (ADM). This ADM contains all relevant aerodynamic information about possible flight states of the SAGITTA demonstrator within its flight envelope. For the ADM, a very comprehensive data set has been created, which is henceforward to be used within the SAGITTA research program for further designing the demonstrator configuration.

The generated experimental data set has additionally validated the CFD computations for the clean configuration with and without attached vertical tails presented in this publication. Hence, the general validity of the numerical analyses has hereby been confirmed. In order to compare the results more thoroughly, new CFD data conducted at a Reynolds number comparable to the wind tunnel experiments would be of particular interest. In this case, questions concerning Reynolds number dependencies could be analyzed in a much more detailed way.

Moreover, the understanding of the asymmetries obtained within the experimental measurements should be investigated more intensively. For this analysis, further detailed wind tunnel experiments would be necessary to study the asymmetric effects discussed in this paper.

ACKNOWLEDGEMENTS

The support of this investigation by EADS CASSIDIAN within the SAGITTA demonstrator program is gratefully acknowledged. Moreover, the authors would like to thank the SAGITTA partners for the fruitful and excellent co-operation.

The computer resources for the CFD computations presented in this publication have been provided by the Gauss Center for Supercomputing/Leibnitz Supercomputing Center (SuperMIG/SuperMUC) in Garching bei München.

Furthermore, the authors thank the German Aerospace Center (DLR) for providing the DLR TAU-Code used for the numerical investigations carried out in this research project. In addition, thanks goes to CENTAURSoft for its guidance during the mesh generation process.

REFERENCES

[1] SEIFERT, J.: SAGITTA - Nationale Forschungskooperation für fortschrittliche UAV-Technologien im Rahmen der Open Innovation Initiative von Cassidian. In: *61th Deutscher Luft- und Raumfahrtkongress, Berlin, Germany, September 10-12, 2012* (DGLR Paper 2012-1352)

[2] ÖZGER, E.: Aerodynamic Model Validation of Unmanned Research Demonstrator SAGITTA. In: *61th Deutscher Luft- und Raumfahrtkongress, Berlin, Germany, September 10-12, 2012* (DGLR Paper 2012-1253)

[3] HOLDAWAY, G.H. ; J.A.MELLENTHIN: Investigation at Mach Numbers of 0.20 to 3.50 of Blended Wing-Body Combinations of Sonic Design with Diamond, Delta and Arrow Plan Forms. In: *NASA Technical Memorandum X-372, 1960*

[4] HUANG, X.Z. ; MÉBARKI, Y. ; BENMEDDOUR, A. ; BROWN, T.: Experimental and Numerical Studies of Geometry Effects on UCAV's Aerodynamics. In: *42th AIAA Aerospace Sciences Meeting & Exhibit, Reno, NV (USA), January 5-8, 2004* (AIAA Paper 2004-403)

[5] HUMMEL, D.: Untersuchungen über das Aufplatzen der Wirbel an schlanken Deltaflügeln. In: *Z. Flugwiss. 13 (1965), No. 5, pp. 158-169*

[6] FURMAN, A. ; BREITSAMTER, C.: Turbulent and Unsteady Flow Characteristics of Delta Wing Vortex Systems. In: *46th AIAA Aerospace Sciences Meeting & Exhibit, Reno, NV (USA), January 7-10, 2008* (AIAA Paper 2008-381)

[7] FRITZ, W. ; CUMMINGS, R.M.: What was Learned From the Numerical Simulations for the VFE-2. In: *46th AIAA Aerospace Sciences Meeting & Exhibit, Reno, NV (USA), January 7-10, 2008* (AIAA Paper 2008-399)

[8] HUMMEL, D.: On the Vortex Formation Over a Slender Wing at Large Angles of Incidence. In: *High Angle of Attack Aerodynamics, Sandefjord, Norway, October 4-6, 1978* (AGARD Paper 1978-247)

[9] GURSUL, I. ; GORDNIER, R. ; VISBAL, M.: Unsteady Aerodynamics of Non-Slender Delta Wings. In: *Progress in Aerospace Science 41 (2005), No. 1, pp. 515-557*

[10] STADLBERGER, K.: Design Drivers for Novel Flight Control Effectors for Low Aspect Ratio Flying-Wing Configurations. In: *61th Deutscher Luft- und Raumfahrtkongress, Berlin, Germany, September 10-12, 2012* (DGLR Paper 2012-1272)

[11] BOUGAS, L.: Propulsion System Integration and Thrust Vectoring Aspcets for Scaled Jet UAVs. In: *61th Deutscher Luft- und Raumfahrtkongress, Berlin, Germany, September 10-12, 2012* (DGLR Paper 2012-1301)

[12] DLR INSTITUTE OF AERODYNAMICS AND FLOW TECHNOLOGY: Technical Documentation of the DLR TAU-Code Release 2010.2.0

[13] SPALART, P.R. ; ALLMARAS, S.R.: One-Equation Turbulence Model for Aerodynamic Flow. In: *30th AIAA Aerospace Sciences Meeting & Exhibit, Reno, NV (USA), January 6-9, 1992* (AIAA Paper 1992-439)